WELDING RESEARCH

SUPPLEMENT TO THE *WELDING JOURNAL*, MAY 1995
Sponsored by the American Welding Society and the Welding Research Council

A Study on the Effect of Contact Tube-to-Workpiece Distance on Weld Pool Shape in Gas Metal Arc Welding

Experiments establish contact tube-to-workpiece distance as an important variable in shaping weld geometry

BY J. -W. KIM AND S. -J. NA

ABSTRACT. Computer simulations of the three-dimensional heat transfer and fluid flow in gas metal arc (GMA) welding have been studied for analyzing the effect of contact tube-to-workpiece distance on the weld pool shape by considering the driving forces for weld pool convection, the electromagnetic force, the buoyancy force and the surface tension force at the weld pool surface, and also the effect of molten electrode droplets. In the numerical simulation, difficulties associated with the irregular shape of the weld bead have been successfully overcome by adopting a boundary-fitted coordinate system that eliminates the analytical complexity at the weld pool and bead surface boundary. The method used in this paper has the capacity to determine the weld bead and penetration profile by solving the surface equation and convection equations simultaneously.

The experiments are performed to show the variation of the weld bead geometry due to the change of the contact tube-to-workpiece distance. The calculated weld shapes correspond well with those of experiments, and both these results demonstrate that the contact of tube-to-workpiece distance exerts a considerable influence on the formation of the weld pool and the resulting weld shape by affecting the arc length and welding current.

J. -W. KIM is an Assistant Professor at Youngnam University, and S. -J. NA is a Professor at Korea Advanced Institute of Science and Technology, Taejon, Korea.

KEY WORDS

Weld Pool Shape
GMAW
Fluid Flow
Heat Transfer
3-Dimensional Model
Boundary-Fit. Coord.
Surface Deformation
Arc Length Distance
Velocity Field
Filler Metal Effect

Introduction

The strength of the weld joint depends upon the size of welds, when the strength of the weld metal is given. In order to get the proper weld size, specific values are assigned to the process variables which control the formation of the weld by influencing the depth of penetration, the bead width, and the bead height. Variation of the welding power and effective radii of the welding heat flux and current path distribution due to the change of the contact tube-to-workpiece distance can affect the weld pool formation and eventually the weld geometry. And because of the large amount of the heat supplied at the weld site over a short period of time, there are many problems in and around a welded joint such as generation of distortion, residual stress, and reduced strength (Ref. 1). Accurate predictions of the weld size and the above problems require a precise analysis of the weld thermal cycle. The importance of a good model for the weld pool convection in the analysis of the thermal cycle has been emphasized by a number of investigators.

A number of researchers have shown that the convection in the weld pool can strongly affect the weld pool geometry and consequently the quality of the resultant welds including the joint penetration, undercutting, and porosity (Refs. 2–11). In recent years, considerable progress has been made, mainly for gas tungsten arc (GTA) welding processes, in modeling the fluid flow and heat transfer condition of weld pools.

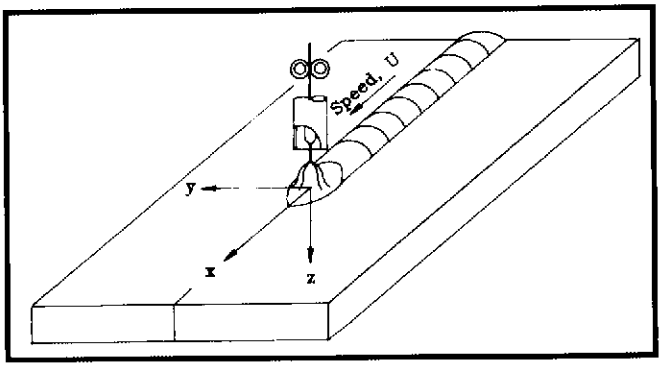

Fig. 1 — Schematic sketch of GMA welding system.

consequently, the weld bead surface. Boundary-fitted coordinate systems, employed in conjunction with finite difference techniques, remove some of the difficulties encountered in representing the complex geometries with the Cartesian or cylindrical polar coordinate system.

The early studies of the fluid flow in weld pools (Refs. 2-4) described the steady-state and electromagnetically driven flows in predetermined hemispherical regions. In an important study on the fluid flow and heat transfer conditions in a stationary GTA weld pool, Oreper, *et al.* (Ref. 5), considered the effect of the surface tension gradient on the weld pool convection for the first time. The surface tension effect on the weld pool geometry has been experimentally investigated by Heiple, *et al.* (Ref. 6). Kou, *et al.* (Ref. 7), presented the results of a quasi-steady, three-dimensional computer model for the flow and heat transfer conditions in the weld pool of the GTA welding process. An inherent limitation in all the aforementioned modeling efforts of the GTA welding process is the assumption that the weld pool surface is nondeformable or flat. A study by Tsao, *et al.* (Ref. 8), presented a two-dimensional stationary weld pool convection model for the GMA welding process, which also adopted the assumption of the flat weld pool surface. More recently, Kim, *et al.* (Ref. 9), studied the phase change problem at the liquid-solid interface and the deformation problem at the weld pool surface in the stationary GTA welding process by adopting a boundary-fitted coordinate system. The three-dimensional computer model based on the deformable surface condition was formulated first by Zacharia, *et al.* (Refs. 10, 11), for the fluid flow and heat transfer analysis in the weld pool of the GTA welding process. But the deformed pool surface was approximated by small steps of the finite difference grids closest to the pool surface.

Molten surface deformation, particularly in the case of GMA welding, plays a significant role in the actual weld bead size and should be considered in order to evaluate the weld pool convection accurately. In this study, a boundary-fitted coordinate was chosen to handle the largely deformed weld pool surface and,

The work presented here considers the three-dimensional quasi-steady heat and fluid flow analysis for the moving heat source of the GMA welding process in which the driving forces for the weld pool convection, the electromagnetic force, the buoyancy force and the surface tension force at the weld pool surface, and also the effect of molten electrode droplets are investigated. The relation of the contact tube-to-workpiece distance to the arc length is discussed for analyzing the effect of the contact tube-to-workpiece distance on the weld pool formation. A series of experiments has been performed to show the variation of the weld geometry due to the change of the contact tube-to-workpiece distance. Numerical simulations have been performed for analyzing the behavior of a quasi-steady GMA weld pool so as to define the principal operating parameters governing the fluid flow and heat transfer phenomena and to investigate the effect of the contact tube-to-workpiece distance on the weld pool shape.

Contact Tube-to-Workpiece Distance in GMA Welding

Arc Behavior and Weld Shape

Among the welding variables, the arc length, which is related with the welding voltage and contact tube-to-workpiece distance, has a close relationship with the weld bead width. Generally, the bead width increases, as the arc length is increased. This can be explained by considering the characteristics of the welding arc. The welding arc has a point-to-plane relationship and is thus bell-like in shape with the point at the end of the electrode and the wide portion at the surface of the weld (Ref. 12). Increasing the arc length makes the bead wider due to the widened arc area at the weld surface, and consequently reduces the reinforcement height because the same volume of the filler metal is involved. Conversely, reducing the arc length makes the bead narrower and increases the height of the reinforcement.

In GMA welding systems, the power source has a flat or constant voltage characteristic and the electrode wire is fed into the arc at a fixed speed. The major reason for selecting the constant voltage source is the self-regulating character inherent in this system. The constant voltage system compensates for the variation in the contact tube-to-workpiece distance, which readily occurs during welding, by automatically supplying the increased or decreased welding current to attain an equilibrium. The power source provides the proper current so that the melting rate is equal to the wire feed rate.

As the contact tube-to-workpiece distance increases, the arc length increases and the welding current decreases momentarily, as the characteristic of the constant voltage power source predicts. However, this also decreases the electrode melting rate. With high-conductivity electrode materials such as aluminum or copper alloys, the resistance and the voltage drop in the electrode extension can be considered as negligible. Therefore, the decreased melting rate and the constant wire feed speed bring the welding current and the arc length back to the normal condition (Ref. 13).

For the ferrous electrode, however, the change of the contact tube-to-workpiece distance eventually influences the welding current. Increasing the contact tube-to-workpiece distance reduces the welding current due to the increased resistance in the circuit. The resistance in the electrode extension of the steel wire plays an important role in the generation of the Joule heat and then affects the melting phenomena. It has been reported that the temperature of molten droplets is lower in the case of the long electrode extension than that of the short electrode extension (Ref. 14). This indicates that the high temperature of the electrode extension promotes the detachment of droplets from the electrode end. The increased contact tube-to-workpiece distance consequently brings on a reestablished equilibrium state of a somewhat extended contact tube-to-workpiece (Ref. 13).

Thus, it can be expected that the contact tube-to-workpiece distance affects the weld bead geometry as well as the arc length. Moreover, the variation of the welding power due to the change of the contact tube-to-workpiece distance can affect the weld pool formation and eventually the weld pool shape. A series of experiments were performed to study the effect of the contact tube-to-workpiece distance on the weld pool shape.

Experiment

In order to show the variation of the weld bead geometry due to the change of the contact tube-to-workpiece distance, a series of experiments was performed for various contact tube-to-workpiece distances. The welding power source used was a standard commercial unit and the welding gun was mounted directly on a computer-controlled single-axis motion table. Welding was done in the flat position, with the vertical gun moving at a prespecified constant speed along the stationary workpiece.

The following welding conditions were selected for experiments:

Tip-to-workpiece distance: 15, 20, and 25 mm; wire feed speed: 150 mm/s; welding speed: 7 mm/s; welding voltage: 31.5 V; wire diameter: 1.2 mm; shielding gas: 80% Ar - 20% CO_2.

The electrode wire of the type of AWS ER70S-3 was used for the mild steel workpieces. The weld geometries were determined by sectioning the resulting weldment. These cut specimens were polished and etched, and then a macro-picture of the weld was taken to measure the weld size.

Formulation

Governing Equations

Figure 1 shows the schematic diagram of the GMA welding process, in which the heat source is moving at a constant speed U, and a constant supply of the consumable electrode is maintained through the center of the welding nozzle. The coordinate system (x, y, z) moves with the heat source at the same speed, and its origin coincides with the center of the electrode.

The molten pool convection was considered as laminar and incompressible (Refs. 7–11). And the following additional assumptions were adopted for the further simplification:

1) Physical properties are constant except for the thermal conductivity, the specific heat and the density in the buoyancy term (Boussinesq approximation).

2) Heat, current and pressure distributions of the arc have Gaussian characteristics.

The governing equations, describing the continuity equation, the momentum equation and the energy equation for steady-state velocity and temperature fields in the workpiece, may then be written as follows:

$$E_x + F_y + G_z = S \tag{1}$$

where

$$E = \begin{Bmatrix} \rho u \\ \rho uu - \mu u \\ \rho uv - \mu v^x \\ \rho uw - \mu w^x \\ \rho cuT - kT_x^x \end{Bmatrix}, \quad F = \begin{Bmatrix} \rho v \\ \rho vu - \mu u \\ \rho vv - \mu v^y \\ \rho vw - \mu w^y \\ \rho cvT - kT_y^y \end{Bmatrix}$$

$$G = \begin{Bmatrix} \rho w \\ \rho wu - \mu u \\ \rho wv - \mu v^z \\ \rho ww - \mu w^z \\ \rho cwT - kT_z^z \end{Bmatrix} \text{ and } S = \begin{Bmatrix} 0 \\ -p_x + f^x \\ -p_y + f^y \\ -p_z + f^z \\ 0^z \end{Bmatrix}$$

There are three distinct driving forces for the weld pool convection, *i.e.*, the electromagnetic force, the buoyancy force and the surface tension gradient at the weld pool surface. The first driving force is caused by the interaction between the divergent current path in the weld pool and the magnetic field it generates. The second driving force is caused by the temperature gradient within the weld pool, and the third by the temperature gradient at the weld pool surface.

In the case of the current flux falling on the flat surface, the analytical solution of the electromagnetic force can be successfully obtained by using the Bessel functions (Ref. 7). According to the com-

$$\text{where } J^r = \frac{I}{2\pi}\int_0^\infty \lambda J_1(\lambda r)\cdot Exp\left(\frac{\lambda^2 b^2}{12}\right)\cdot \frac{\cosh \lambda(H-\hat{z})}{\sinh(\lambda H)}d\lambda,\ J^z = \frac{I}{2\pi}\int_0^\infty \lambda J_0(\lambda r)\cdot Exp\left(\frac{\lambda^2 b^2}{12}\right)\cdot \frac{\sinh \lambda(H-\hat{z})}{\sinh(\lambda H)}d\lambda,\ B^\theta = \frac{\mu_m I}{2\pi}\int_0^\infty \lambda J_1(\lambda r)\cdot Exp\left(\frac{\lambda^2 b^2}{12}\right)\cdot \frac{\sinh \lambda(H-\hat{z})}{\sinh(\lambda H)}d\lambda$$

putational analysis of Tsai, *et al.* (Ref. 12), for the deformed surface, the electromagnetic force at a point 2.5 mm (0.1 in.) apart from the origin is less than a tenth of the maximum value for the welding current of 150 A in GTA welding. By the result of repeated calculations in this study, the surface deformation within the 3-mm (0.12-in.) radius around the origin was revealed not to be severe. Therefore, the body force in Equation 1 can be expressed by using the approximated electromagnetic force and buoyancy force as follows:

$$f = J \times B - \rho\beta g(T - T_r) \tag{2}$$

where r is the radius, *i.e.*, $\sqrt{x^2+y^2}$, $\hat{z}$ the depth from the weld pool surface, and J_0 and J_1 are the Bessel functions of the first kind and of the zero and first order, respectively. The other components of J and B are zero.

Boundary Conditions

The boundary conditions for the fluid flow and temperature distributions are as follows:

Top surface

$$V \cdot n = 0 \tag{3a}$$

$$\mu\nabla(V \cdot t_1)\cdot n = -\left(\frac{d\sigma}{dT}\right)\nabla T \cdot t_1 \tag{3b}$$

$$\mu\nabla(V \cdot t_2)\cdot n = -\left(\frac{d\sigma}{dT}\right)\nabla T \cdot t_2 \text{ in the weld pool} \tag{3c}$$

$$u = -U,\ v = w = 0 \text{ in the solid region} \tag{3d}$$

$$-k\nabla T \cdot n = h(T - T_\infty) \text{ for } r \geq a$$

$$w^{m+1} = w^m + v_d \text{ at the weld pool surface} \tag{3e}$$

The normal and tangential unit vectors in Equations 3a–3c are determined on the surface node and the equations 3b and 3c represent the boundary conditions for surface tension gradient at the pool surface. Equation 3e is for considering the effect of molten electrode droplets, where m represents the internal iteration number of the calculation loop.

$$-k\nabla T \cdot n = q_a(z \cdot n) \text{ for } r \leq a \tag{4a}$$

(4b)

where z is the unit vector of the z direction and h, a combined heat transfer coefficient for the radiative and convective boundary conditions, which can be calculated from the following relationship (Ref. 1):

$$h = 24.1\times10^{-4}\,\varepsilon\, T^{1.61}\left(W/m^2\,{}^\circ C\right) \tag{5}$$

where ε is the emissivity of the surface of the body. A value of 0.9 was assumed for ε, as recommended for the hot rolled steel (Ref. 16).

Bottom surface

$$u = -U,\ v = w = 0 \tag{6}$$

$$-k\nabla T \cdot n = h(T - T_\infty) \tag{7}$$

Center plane

$$v = 0,\ \frac{\partial u}{\partial y} = \frac{\partial w}{\partial y} = 0 \tag{8}$$

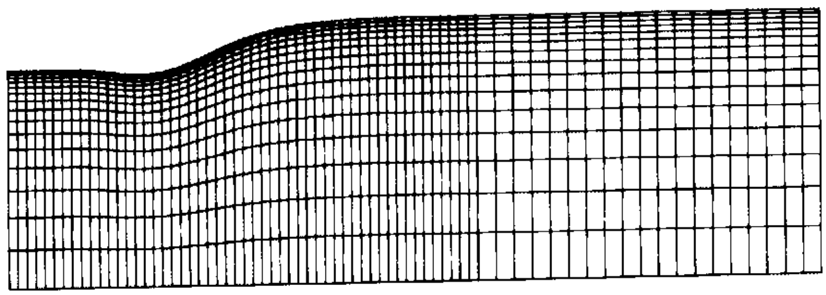

Fig. 2 — An example of grid used (center plane).

$$\frac{\partial T}{\partial y} = 0 \tag{9}$$

Side surface

$$u = -U, \ v = w = 0 \tag{10}$$

$$-k\nabla T \cdot n = h(T - T_\infty) \tag{11}$$

Front surface boundary

$$u = -U, \ v = w = 0 \tag{12}$$

$$T = T_\infty \tag{13}$$

Rear surface boundary

The actual boundary condition of the temperature imposed on the rear boundary surface can be defined only in the case of the infinite calculation domain, where the boundary temperature is equal to the ambient temperature (T_∞). However, the following numerical boundary condition was applied because a finite domain must be used.

$$u = -U, \ v = w = 0 \tag{14}$$

$$T_b = T_i - \left(\frac{\partial T}{\partial x}\right)_i \Delta x \tag{15}$$

where T_b is the temperature of the boundary and the subscript i means the internal node of the boundary. It was assumed in Equation 15 that the temperature gradient is conserved at the rear calculation boundary, which moves with the welding speed (Ref. 17). In calculations, however, the solutions were found not to be very sensitive to this boundary condition.

The solid/liquid interface was treated as the free boundary problem involving the heat and fluid flow. This is due to the fact the solid/liquid interface does not have to be considered as a boundary. The effective-viscosity method was used for the equation of motion, in conjunction with a viscosity-temperature relationship covering both the solid and liquid phase. Since no fluid flow exists in the solid phase, the very large viscosity was applied to the solid region. The pool boundary was then determined by tracing the locations where the temperature corresponds to the liquidus temperature of the workpiece.

Surface Deformation

The weld pool surface under the arc pressure forms a shape which satisfies the equilibrium condition of the surface in the gravitational field. Hence, it is usually convenient to use the condition of equilibrium by directly solving the variational problem subject to the constraint that the volume of the weld pool is constant. For the precise calculation of the surface deformation, the convection in the liquid pool, the electromagnetic force itself, and the effect of metal transfer should be considered. In this study, however, those were assumed to be negligible for simplifying the problem. In a previous study, the effect of convection in the liquid pool was found to be less than that of the arc pressure (Ref. 15). Thus, the total energy to be minimized includes the surface energy connected with the change in the area of the weld surface, the potential energy in the gravitational field, and the work performed by the arc pressure displacing the weld pool surface. The total energy is therefore given by the following equation (Ref. 18):

$$\xi_t = \iint_s \left(\sigma\sqrt{1 + z_x^2 + z_y^2} + \frac{1}{2}\rho g z^2 - p_{arc} z \right) dx\,dy \equiv \iint_s F\,dx\,dy \tag{16}$$

where s means the surface of the workpiece.

Since the volume of the fed wire is additionally supplied in GMA welding (V_w), the constraining equation is as follows:

$$\iint_s -z\,dx\,dy \equiv \iint_s G\,dx\,dy = V_w \tag{17}$$

The necessary condition for the solution follows from the application of the appropriate Euler equation.

$$\frac{\partial}{\partial x}\left\{\frac{\partial}{\partial z_x}(F + \lambda G)\right\} + \frac{\partial}{\partial y}\left\{\frac{\partial}{\partial z_y}(F + \lambda G)\right\} - \frac{\partial}{\partial z}(F + \lambda G) = 0 \tag{18}$$

Substitution of the values previously defined into the Euler equation gives a somewhat complex form of the equation, because the surface tension σ is position dependent in the distributed temperature field. But the derivative term of the surface tension is as small as about a factor of 100 less than that of the other terms. Ignoring the derivative term of the surface tension, the following equation can be derived.

$$\sigma\left\{\frac{(1 + z_y^2)z_{xx} - 2z_x z_y z_{xy} + (1 + z_x^2)z_{yy}}{(1 + z_x^2 + z_y^2)^{3/2}}\right\} = \rho g z - p_{arc} - \lambda \tag{19}$$

where the surface tension σ at the weld pool surface was assumed to vary with the temperature as follows (Ref. 19):

$$\sigma(T) = \sigma(T_l) + (d\sigma / dT)(T - T_l)\ N/m \tag{20}$$

The radial distribution of the arc pressure p_{arc} employed was adopted from the reference (Ref. 20). In the computational procedure, the iterative method of the finite difference has been used to solve the nonlinear differential Equation 19. After these calculations, the computational result is applied to the constraint prescribed. If it does not satisfy the constraining equation, the computation should be repeated after modification of Lagrange multiplier λ in Equation 19. The value of λ is modified by using the golden section search technique (Ref. 21).

Numerical Procedure

Transformation

Boundary-fitted coordinate systems, employed in conjunction with the finite difference technique, remove the difficulties encountered in representing the complex geometries with the Cartesian or cylindrical polar coordinate system (Ref. 22). In the boundary-fitted coordinate system, the finite difference grid lines are aligned with the surface boundaries so that the interpolation of flow variables and the representation of normal derivatives at boundaries can be performed accurately. If a regular finite difference grid is used to represent the complex geometries, the boundaries intersect the grid lines, which makes the computer programming complex and the evaluation of derivatives inaccurate.

In order to gain a better accuracy, a grid mesh with variable spacing was employed. The grid spacings are fine near the location of the heat source and coarsened with distance away from it. An example of such a grid mesh is shown in Fig. 2 for the center (y = 0 mm) plane. In a boundary-fitted coordinate method, the physical geometry is transformed into a rectangular, uniformly spaced finite difference mesh.

Equation 1 is transformed to a general curvilinear coordinate system (ξ, η, ζ), which results in Equation 21.

$$E_\xi \xi_x + E_\eta \eta_x + E_\zeta \zeta_x + F_\xi \xi_y + F_\eta \eta_y + F_\zeta \zeta_y + G_\xi \xi_z + G_\eta \eta_z + G_\zeta \zeta_z = S \tag{21}$$

where $\xi_x = I_t\left(y_\eta z_\zeta - y_\zeta z_\eta\right),$

$\xi_y = -I_t\left(x_\eta z_\zeta - x_\zeta z_\eta\right),$

$\xi_z = I_t\left(x_\eta y_\zeta - x_\zeta y_\eta\right),$

$\eta_x = -I_t\left(y_\xi z_\zeta - y_\zeta z_\xi\right),$

$\eta_y = I_t\left(x_\xi z_\zeta - x_\zeta z_\xi\right),$

$\eta_z = -I_t\left(x_\xi y_\zeta - x_\zeta y_\xi\right),$

$\zeta_x = I_t\left(y_\xi z_\eta - y_\eta z_\xi\right),$

$\zeta_y = -I_t\left(x_\xi z_\eta - x_\eta z_\xi\right),$

$\zeta_z = I_t\left(x_\xi y_\eta - x_\eta y_\xi\right),$

$$I_t = 1 / \left\{ \begin{array}{l} x_\xi\left(y_\eta z_\zeta - y_\zeta z_\eta\right) - \\ x_\eta\left(y_\xi z_\zeta - y_\zeta z_\xi\right) - \\ x_\zeta\left(y_\xi z_\eta - y_\eta z_\xi\right) \end{array} \right\}$$

$$\text{and } S_1 = \left\{ \begin{array}{l} 0 \\ -\left(p_\xi \xi_x + p_\eta \eta_x + p_\zeta \zeta_x\right) + f^X \\ -\left(p_\xi \xi_y + p_\eta \eta_y + p_\zeta \zeta_y\right) + f^Y \\ -\left(p_\xi \xi_z + p_\eta \eta_z + p_\zeta \zeta_z\right) + f^Z \\ 0 \end{array} \right\}$$

where $\xi_x = I_t\left(y_\eta z_\zeta - y_\zeta z_\eta\right),$

$\xi_y = -I_t\left(x_\eta z_\zeta - x_\zeta z_\eta\right),$

$\xi_z = I_t\left(x_\eta y_\zeta - x_\zeta y_\eta\right),$

The transformation coefficients, ξ_x, ξ_y, ξ_z, η_x, η_y, η_z, ζ_x, ζ_y and ζ_z, are determined numerically using the second order central differencing technique on the grid generated to fit the irregular boundaries. In the transformed domain the grid sizes (*i.e.*, $\Delta\xi$, $\Delta\eta$ and $\Delta\zeta$) are set to be unity to simplify the calculation of transformation coefficients.

The governing Equation 21 can be represented by the following transport equation in which φ denotes all the dependent variables and Γ the diffusion coefficient:

$$\left\{\rho u\phi - \Gamma\left(\phi_\xi \xi_x + \phi_\eta \eta_x + \phi_\zeta \zeta_x\right)\right\}_\xi \xi_x +$$
$$\left\{\rho u\phi - \Gamma\left(\phi_\xi \xi_x + \phi_\eta \eta_x + \phi_\zeta \zeta_x\right)\right\}_\eta \eta_x +$$
$$\left\{\rho u\phi - \Gamma\left(\phi_\xi \xi_x + \phi_\eta \eta_x + \phi_\zeta \zeta_x\right)\right\}_\zeta \zeta_x +$$
$$\left\{\rho v\phi - \Gamma\left(\phi_\xi \xi_y + \phi_\eta \eta_y + \phi_\zeta \zeta_y\right)\right\}_\xi \xi_y +$$
$$\left\{\rho v\phi - \Gamma\left(\phi_\xi \xi_y + \phi_\eta \eta_y + \phi_\zeta \zeta_y\right)\right\}_\eta \eta_y +$$
$$\left\{\rho v\phi - \Gamma\left(\phi_\xi \xi_y + \phi_\eta \eta_y + \phi_\zeta \zeta_y\right)\right\}_\zeta \zeta_y +$$
$$\left\{\rho w\phi - \Gamma\left(\phi_\xi \xi_z + \phi_\eta \eta_z + \phi_\zeta \zeta_z\right)\right\}_\xi \xi_z +$$
$$\left\{\rho w\phi - \Gamma\left(\phi_\xi \xi_z + \phi_\eta \eta_z + \phi_\zeta \zeta_z\right)\right\}_\eta \eta_z +$$
$$\left\{\rho w\phi - \Gamma\left(\phi_\xi \xi_z + \phi_\eta \eta_z + \phi_\zeta \zeta_z\right)\right\}_\zeta \zeta_z = S_1 \tag{22}$$

Numerical Scheme

Discretization of Equation 22 is performed by using the finite difference approximation in the transformed domain. The second order central differencing technique is used for approximating the diffusion and the source terms. For the convection terms, the hybrid differencing scheme (Ref. 23) is employed. The finite difference equation is arranged by collecting the terms according to the grid nodes around a control volume as shown in Fig. 3. The final expression is given by Equation 23 in which A represents the link coefficients between grid nodes:

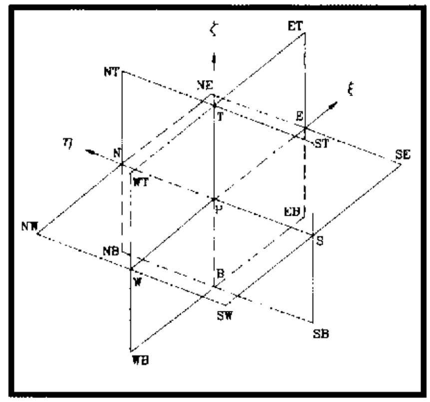

Fig. 3 — Grid structure and labeling around a grid node p.

$$A_P \phi_P = A_E \phi_E + A_W \phi_W + A_N \phi_N + A_S \phi_S + A_T \phi_T + A_B \phi_B + S' \tag{23}$$

Table 1 — Parameters Used in Computations

ρ = 7200 kg/m³	T_∞ = 20°C
μ = 0.006 kg/m s	T_l = 1520°C
β = 10^{-4} K^{-1}	T_v = 2500°C
μ_m = 0.26 × 10^{-6} H/m	H = 12 mm
$d\sigma/dT$ = 10^{-5} N/m °C	U = 7 mm/s

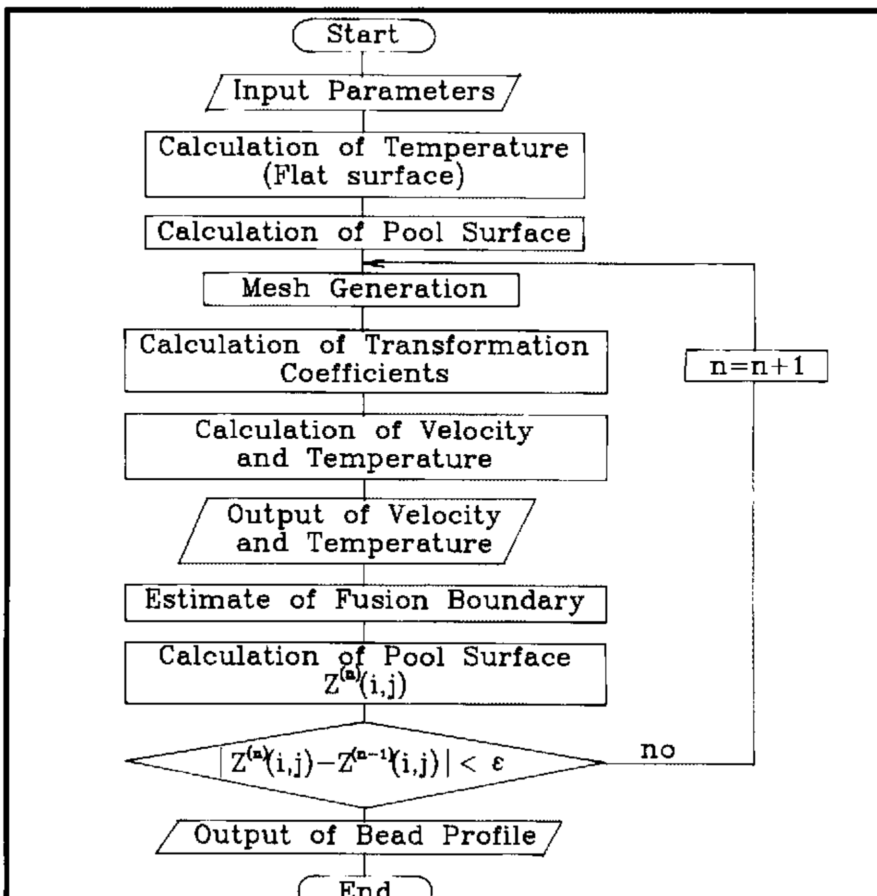

Fig. 4 — Flow chart of calculations.

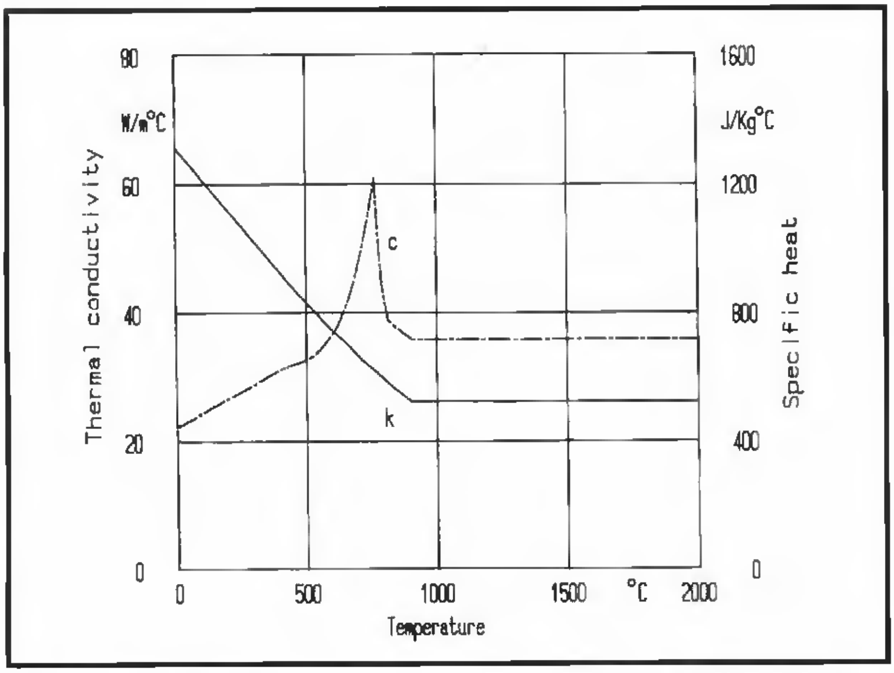

Fig. 5 — Temperature-dependent thermal conductivity and specific heat of AISI 1010 (Ref. 16).

Table 2 — Measured Weld Sizes and Welding Currents According to Various Contact Tip-to-Workpiece Distances (L)

L (mm)	Bead Width (mm)	Bead Height (mm)	Joint Penetration (mm)	Welding Current (A)
15	11.32	3.12	5.05	300
20	12.60	2.82	3.95	280
25	13.20	2.79	2.84	260

Table 3 — Welding Parameters Relevant to Contact Tube-to-Workpiece Distance Variation (L)

Tube-to-Workpiece Distance (mm)	a (mm)	b (mm)	c (mm)	e (mm)	P_{max} (kN/m^2)	Q (W)
15	18.0	5.2	5.4	1.6	0.85	6615
20	10.0	6.5	6.0	2.0	0.80	6170
25	12.0	7.8	7.2	2.4	0.75	5733

where

$$S^* = S_l + A_{NE}\phi_{NE} + A_{NW}\phi_{NW} + A_{NT}\phi_{NT} + A_{NB}\phi_{NB} + A_{SE}\phi_{SE} + A_{SW}\phi_{SW} + A_{ST}\phi_{ST} + A_{SB}\phi_{SB} + A_{ET}\phi_{ET} + A_{EB}\phi_{EB} + A_{WT}\phi_{WT} + A_{VB}\phi_{VB}$$

$$A_P = A_E + A_V + A_N + A_S + A_T + A_B$$

Thus, the nonlinear equations of the transportation are approximated by a system of linear algebraic equations.

A velocity-pressure correction algorithm SIMPLE-C (Ref. 24) was used for the solution procedure of the discretized equations. This kind of procedure requires a grid staggering between the velocity or temperature nodes and the locations where the pressure is estimated for the numerical stability in calculations. The unevenly spaced grids 73 x 31 x 17 were used for the 45.5 x 20 x 12-mm (length x width x thickness (H)) calculation domain. The overall solution procedure is shown in Fig. 4, and the welding parameters and the physical properties used in the calculations are shown in Table 1 and Fig. 5. The iterative procedure for the calculation of the velocity and temperature distribution was continued until the following convergence criterion was satisfied:

$$Max.\frac{\left|\phi - \phi^{old}\right|}{\left|\phi\right|} \leq 0.001$$

And the following convergence criterion was used for the overall calculation;

$$\left|z^n - Z^{n-1}\right| \leq 0.01\ mm$$

The typical computer time was about 1600 minutes CPU time on the CRAY2S computer.

Results and Discussion

Experimental Results and Discussion

The results of the experiment were illustrated in Table 2 and Fig. 6, in which the measured weld sizes and pho-

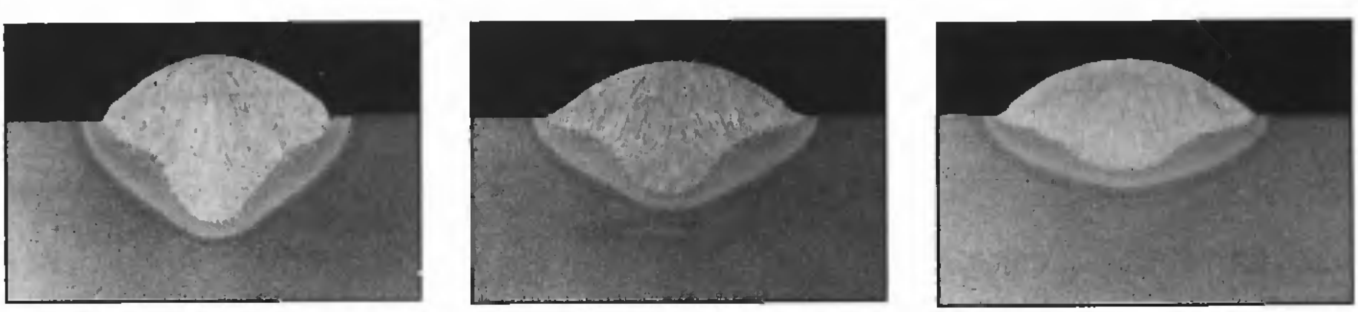

A B C

Fig. 6 — Photographs of weld geometry according to change of contact tube-to-workpiece distance (L). A — L = 15 mm; B — L = 20 mm; C — L = 25 mm.

tographs are represented respectively. A typical finger-like penetration, frequently produced in GMA welding with Ar or its mixture shielding gas, can be seen in all the figures.

The welding current was decreased according to the increasing contact tube-to-workpiece distance as shown in Table 2. The welding current determines the welding power because the welding voltage was kept at a specified value in this experiment. But the largest bead width was acquired in the case of the longest contact tube-to-workpiece distance in spite of the low welding power as shown in the figure. This is probably due to the increased arc length by the increase of the contact tube-to-workpiece distance. Consequently, increasing the arc length makes the bead wider and the reinforcement lower, as mentioned earlier.

It can be also seen in the figure that the depth of joint penetration distinctly increases with the decrease of the contact tube-to-workpiece distance. This is considered to be due to the constriction of the distributed heat and current flux by the decreased arc length, which results in a large electromagnetic force, which promotes the convection effect in the weld pool.

The experiments demonstrate that the contact tube-to-workpiece distance exerts a considerable influence on the formation of the weld pool and the resulting weld shape by affecting the arc length and welding current. The contact tube-to-workpiece distance is thus considered an important variable, which can control the formation of welds.

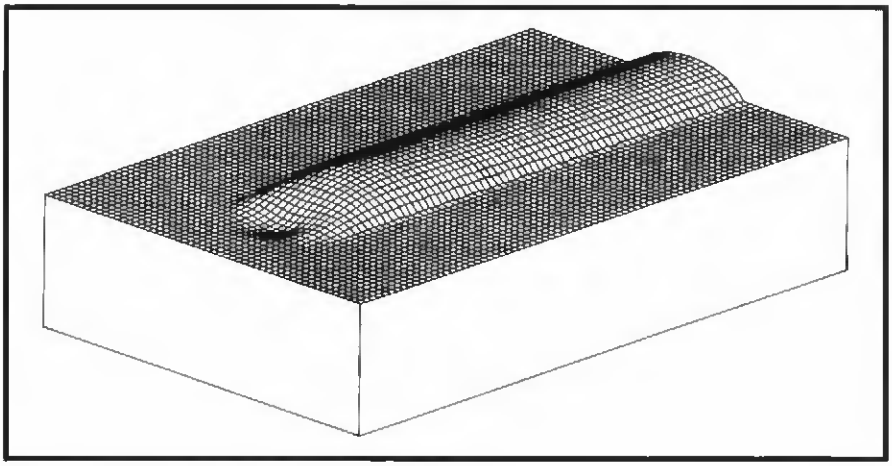

Fig. 7 — An example of calculated weld surface.

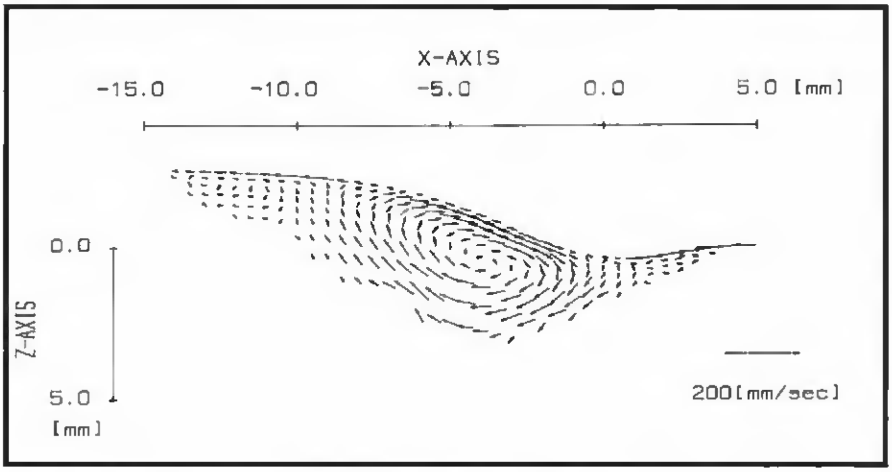

Fig. 8 — Velocity distribution in weld pool (center plane, y = 0 mm).

Calculation Results and Discussion

At certain combinations of welding parameters, the GMA welding process results in a finger-like penetration such as illustrated in Fig. 6. Previous models, which used the conduction model only, were unable to explain the phenomena of this finger-like penetration in the GMA weld. Thus, it is expected that weld pool convection, which causes more heat to be transferred from the heat source to the weld root, plays an important role in the formation of the weld penetration.

Effect of the Three Driving Forces

Calculations were performed by considering the three driving forces, the electromagnetic force, the buoyancy force and the surface tension force at the weld pool. The values of the relevant parameters employed are those from the condition of 20 mm (0.78 in.) contact tube-to-workpiece distance listed in Table 3. A calculated weld surface is illustrated in Fig. 7, where the weld pool deformation due to the gravitation and arc force can be seen. The weld pool surface under the arc center was depressed below the unmelted weld surface.

Figure 8 shows the side view of the fluid flow pattern in the weld pool due to the combined effect of the buoyancy force, the electromagnetic force and the surface tension gradient. As can be seen from the figure, the weld pool has a tail about 15 mm (0.6 in.) long, due to the travel of the heat source. At extremely high welding speeds, the arc may be unsymmetric. But the symmetric arc current and heat distributions were still used for the calculation in this study, because the speeds of the electron movement and plasma flow are much higher than the normal welding speed.

There are two circulation loops in the convection pattern in Fig. 8, one in the middle part and the other in the rear part of the weld pool. The primary circulation loop in the middle part of the weld pool is mainly due to the electromagnetic force. By the interaction between the divergent current path in the weld pool and the magnetic field it generates, a downward electromagnetic force is produced near the z-axis and this force pushes the high-temperature liquid metal in that region downward to the weld pool bottom. The flow pattern induced by the electromagnetic force allows the welding heat to be delivered efficiently from the heat source to the weld root, and consequently results in a deep weld penetration. The second circulation loop in the rear part of the weld pool is mainly due to the surface tension gradient at the pool surface and the effect of the primary circulation. The temperature gradient of the surface tension is generally negative, that is, the surface tension is lower near the center of the weld pool surface, where the temperature is higher, and higher near the pool boundary, where the temperature is lower. Therefore, the liquid

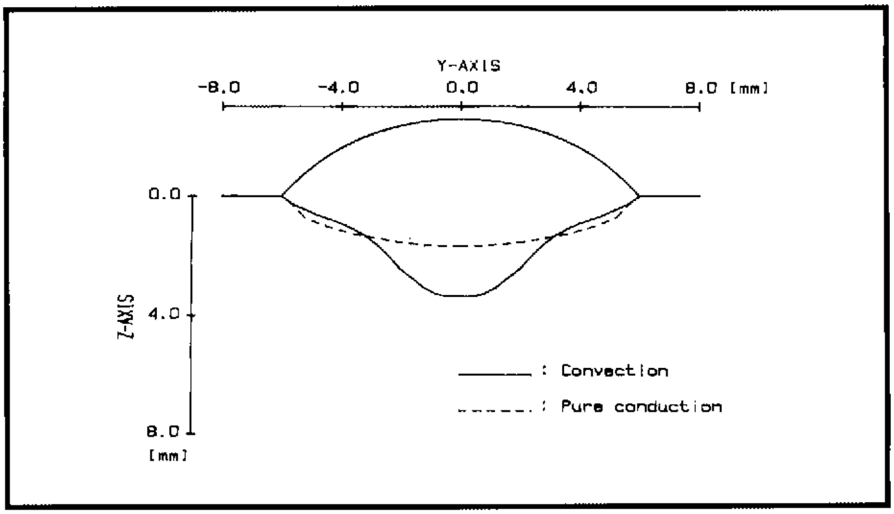

Fig. 9 — Comparison of weld bead shapes for two different calculation methods.

metal near the center of the weld pool surface is driven toward the weld pool boundary.

The detail descriptions for the effect of the three driving forces have been described in the authors' previous study (Ref. 25).

In calculation results of the heat transfer without considering any convective motion in the weld pool, there can be seen no deep penetration shape — Fig. 9. As shown in the figure, it is evident that the liquid metal flow plays a very important role in the formation of the finger-like penetration in GMA welds, and the electromagnetic force is the dominant driving force for the liquid metal flow.

Effect of Molten Electrode Droplets

In GMA welding processes with the spray transfer mode, which is the most common mechanism of the free-flight metal transfer, the molten filler metal is delivered across the arc as fine droplets. Thus, the transferred molten droplets provide an additional heat flow in the weld pool by promoting the fluid motion in the weld pool, compared with the case of considering the three driving forces only. In order to include the effect of molten droplets into the numerical model in this study, it was assumed that the molten electrode is transferred to the weld pool surface with the distributed velocities of the Gaussian characteristics as shown in Fig. 10, where V_r is the volumetric feed rate of the electrode. The effective radius of the velocity distribution was assumed also to be affected by the contact tube-to-workpiece distance as shown in Table 3. The distributed velocities were then added to the converged velocity components of the fluid at the weld pool surface in the iterative calculation procedure.

Figure 11 shows the fluid flow pattern in the weld pool due to the combined effect of the three driving forces and the droplets of the molten electrode. As can be seen from the side view in Fig. 11A, the weld pool length in the weld line direction is longer than that in the case of considering the three driving forces only due to the promoted fluid motion. The magnitude and direction of the fluid velocities, especially under the center of the arc, are considerably different from those in Fig. 5. It was thus presumed that the molten electrode droplets have an influence on the formation of the weld pool by promoting the fluid motion and then on the weld shape. Figure 11B shows the top view of the convection pattern on the weld surface. As shown, the flow at the free surface is outward, from the center to the pool boundary. The temperature gradient at the weld pool surface and consequently the shear stress due to the surface tension gradient are larger in the front part of the arc than that in the rear part. Therefore, high velocities are seen near the front pool boundary, while low velocities are near the rear pool boundary.

The effect of molten electrode droplets on the weld size and shape was represented in Fig. 12 by comparing the calculated weld bead with that in the case of considering the three driving forces only. By considering the molten electrode droplets, the depth of penetration was considerably increased. However, the variation of the velocity distribution radius of the molten electrode shows only a small change of the weld pool shape as shown in Fig. 13 for the employed conditions.

Effect of Contact Tube-to-Workpiece Distance

For investigating the effect of the contact tube-to-workpiece distance on the weld pool formation, the welding parameters relevant to the contact tube-to-workpiece distance variation are selected as shown in Table 3 by considering the results of the arc behavior analysis. From the analysis, it was considered that the increase of the arc length due to the increased contact tube-to-workpiece distance causes the distribution of the heat, current flux and arc pressure to be expanded (Refs. 12, 20, 26).

In the experiment for the contact tube-to-workpiece distance variation, it was revealed that the effect of the contact tube-to-workpiece distance on the weld shape is considerable. Figures 14 and 15 show the fluid flow pattern at the center plane (y = 0 mm) in the weld pool for the

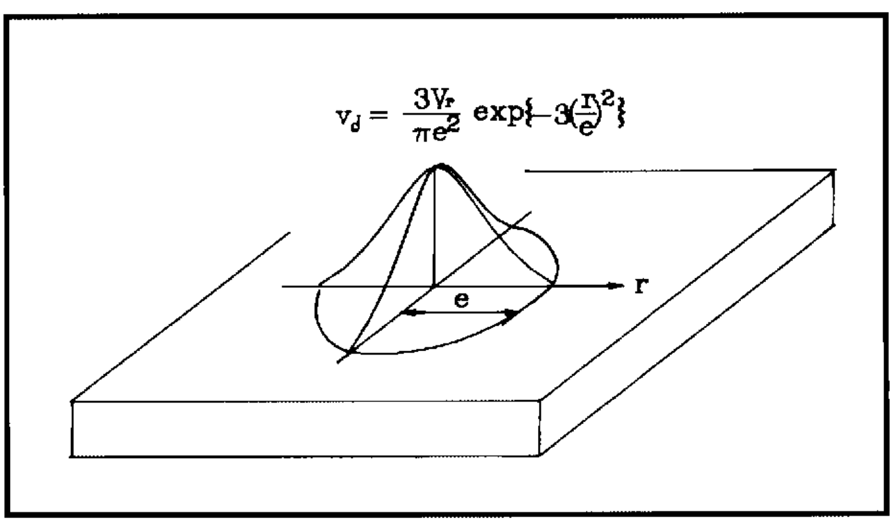

Fig. 10 — Velocity distribution of molten electrode transferred.

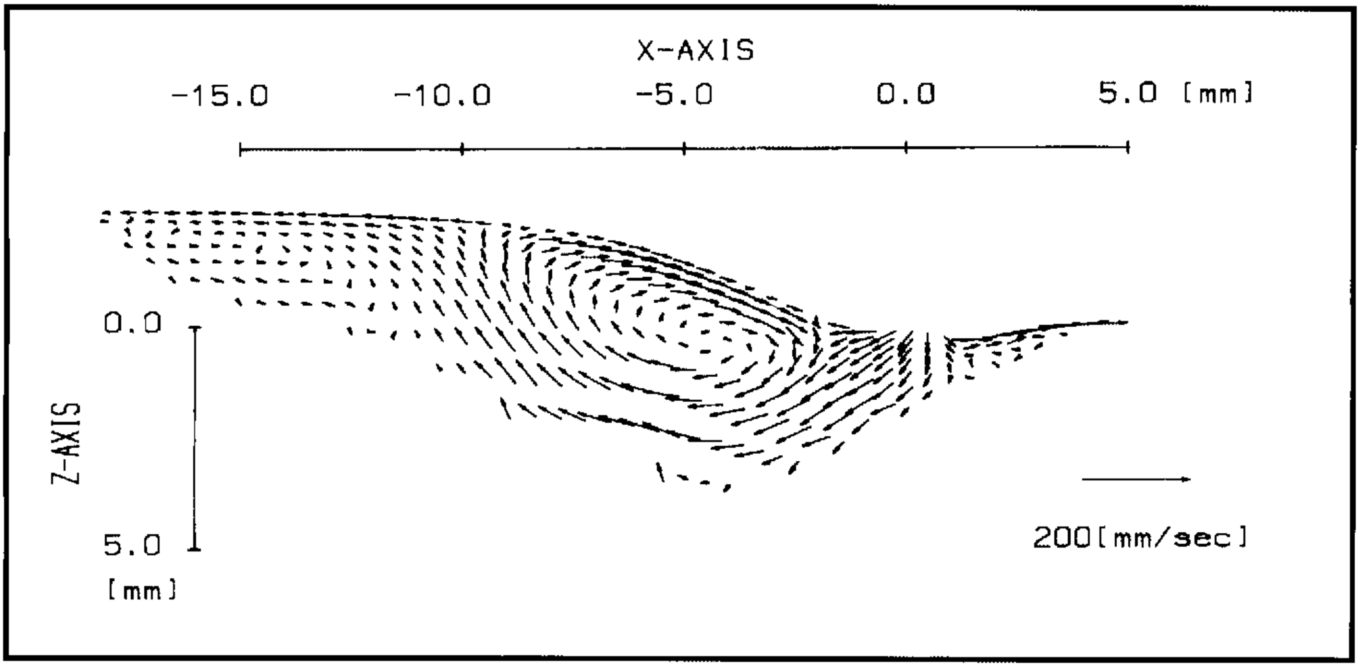

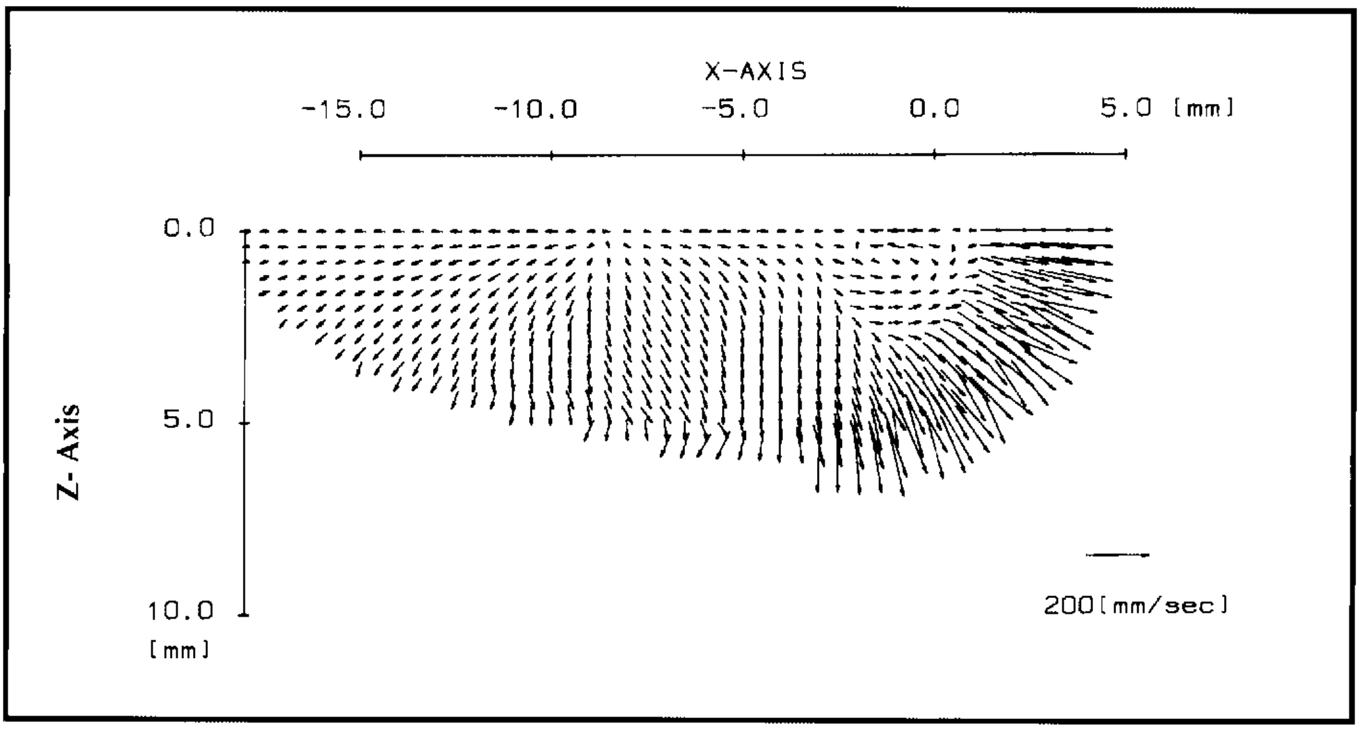

Fig. 11 — Velocity distribution in weld pool by additional effect of molten droplets. A — center plane (y = 0 mm); B — projected top surface.

contact tube-to-workpiece distances of 15 and 25 mm, respectively. As the contact tube-to-workpiece distance decreases, the radii of the welding current flux and distributed velocity of the molten electrode were considered to decrease and consequently the maximum velocity of the fluid motion is increased. Figure 16A–C shows the comparisons between the calculated weld shape and experimental one. The calculated penetration shape was somewhat underestimated in the condition of 15-mm contact tube-to-workpiece distance in comparison with the measured weld shape, but slightly overestimated in the condition of 25-mm contact tube-to-workpiece distance, which is considered to be due to the rough model for transferred molten droplets. In spite of many assumptions and simplifications, however, it is revealed that the calculated weld shapes correspond well with those of the experiments. It can be thus expected that a better model of molten electrode droplets could make the calculation more accurate.

Figure 17 illustrates the effect of the contact tube-to-workpiece distance on the calculated weld shape and shows the considerable variations between the weld shapes as could be also seen in the experimental ones.

Conclusions

A three-dimensional convection

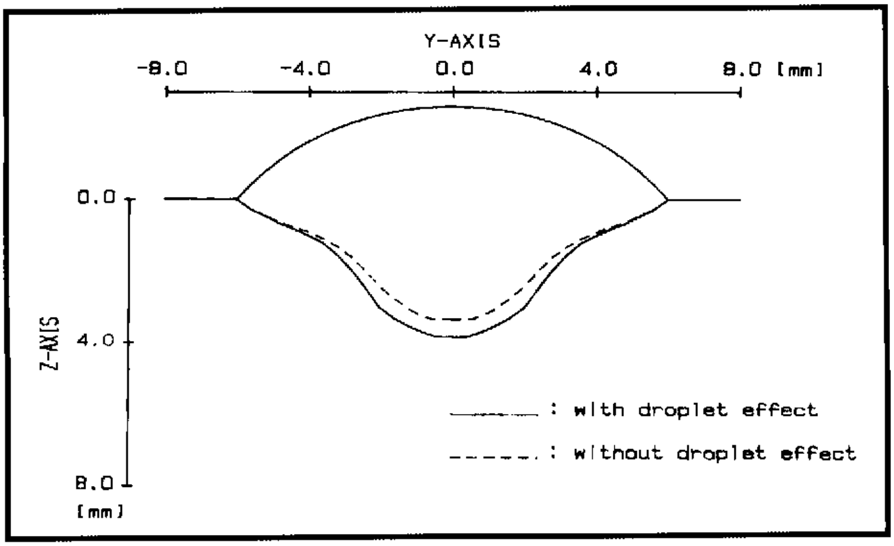

Fig. 12 — Effect of molten droplets on weld shape.

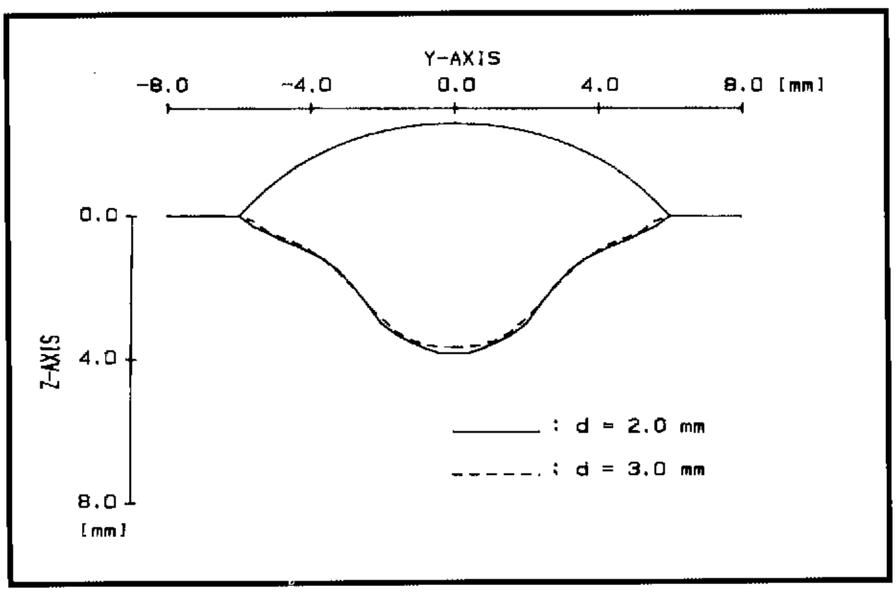

Fig. 13 — Effect of velocity distribution radius of molten droplets on weld shape.

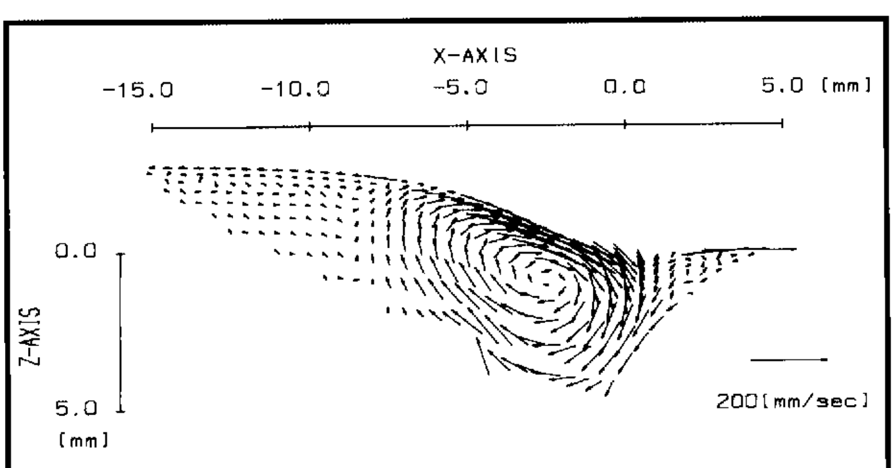

Fig.14 — Velocity distribution at center plane (y = 0 mm) in weld pool (L = 15 mm).

model has been developed to calculate the bead shape, velocity field and temperature field in the GMA weld pool, and then to investigate the effect of the contact tube-to-workpiece distance on the weld shape. In computer modeling, three distinct driving forces for the weld pool convection were considered: the buoyancy force, the electromagnetic force and the surface tension at the weld pool surface. In addition to these, the effect of molten electrode droplets was also considered for the accurate analysis of the process. A boundary-fitted coordinate system was used to handle the deformed weld pool and weld bead surface.

The result of computations has shown that the weld pool has a long tail behind the arc due to the travel of the heat source. The electromagnetic force may have a strong effect on the weld pool convection and consequently on the shape and size of the GMA welds, while the effect of the buoyancy force and the surface tension force at the weld pool surface is relatively small. The primary circulation of the fluid flow was shown in the middle part of the weld pool due to the electromagnetic force, and the outward flow near the pool boundary of the free surface due to the surface tension gradient. The narrow and deep joint penetration could be acquired in the result of calculations by considering the weld pool convection, which cannot be seen in the calculation result of the heat transfer without considering any convective motion. As the effective radius of the current distribution decreases, an increase in the weld pool penetration can be also expected. By considering the molten electrode droplets, which promotes the fluid motion in the weld pool, the depth of penetration was considerably increased in comparison with that in the case of considering the three driving forces only. In spite of many assumptions and simplifications, it was seen that the calculated weld shapes correspond well with those of experiments.

From the experiment and calculation results, it was revealed that the contact tube-to-workpiece distance exerts a considerable influence on the formation of the weld pool and then the weld bead shape by affecting the arc length and welding current. The contact tube-to-workpiece distance is thus considered as one of the important variables that controls the formation of the GMA welds.

References

1. Goldak, J., Bibby, M., Moore, J., House, R., and Patel, B. 1986. Computer modeling of heat flow in welds. *Metall. Trans.* 17B(9):

587–600.
2. Sozou, C., and Pickering, W. M. 1976. Magnetohydrodynamic flow due to the discharge of an electric current in a hemispherical container. *J. Fluid Mechanics* 73: 641–650.
3. Andrews, J. G., and Craine, R. E. 1978. Fluid flow in a hemisphere induced by a distributed source of current. *J. Fluid Mechanics* 84: 281–290.
4. Atthey, D. R. 1980. A mathematical model for fluid flow in a weld pool at high currents. *J. Fluid Mechanics* 98: 787–801.
5. Oreper, G. M., and Szekely, J. 1984. Heat- and fluid-flow phenomena in weld pools. *J. Fluid Mechanics* 147: 53–79.
6. Heiple, C. R., and Roper, J. R. 1982. Mechanism for minor element effect on GTA fusion zone geometry. *Welding Journal* 61(4): 97-s to 102-s.
7. Kou, S., and Wang, Y. H. 1986. Computer simulation of convection in moving arc weld pools. *Metall. Trans.* 17A(12): 2271–2277.
8. Tsao, K. C., and Wu, C. S. 1988. Fluid flow and heat transfer in GMA weld pools. *Welding Journal* 67(3): 70-s to 75-s.
9. Kim, S. D., and Na, S. J. 1989. A study on heat and mass flow in stationary gas tungsten arc welding using the numerical mapping method. *Proc. Inst. Mech. Engrs. Part B — J. Engineering Manufacture* 203:233–242.

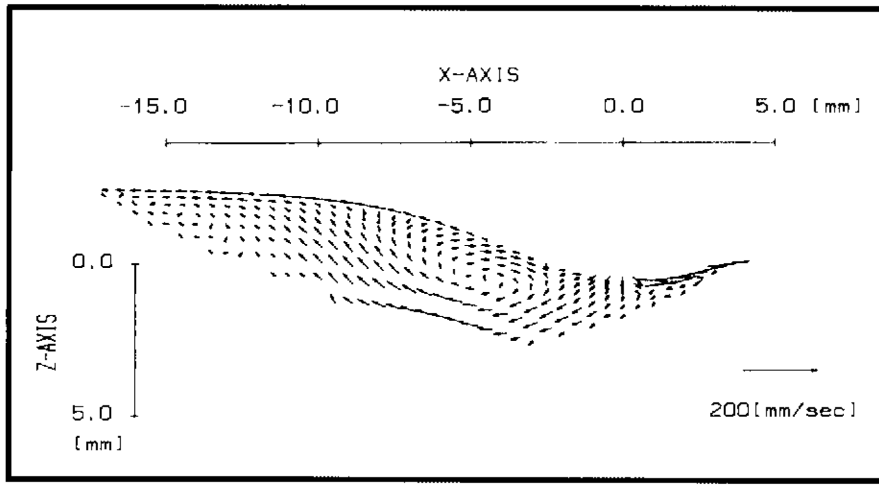

Fig. 15 — Velocity distribution at center plane (y = 0 mm) in weld pool (L = 25 mm).

10. Zacharia, T., Eraslan, A. H., and Aidun, D. K. 1988. Modeling of autogenous welding. *Welding Journal* 67(3): 53-s to 62-s.
11. Zacharia, T., Eraslan, A. H., and Aidun, D. K. 1988. Modeling of nonautogenous welding. *Welding Journal* 67(1): 18-s to 27-s.
12. Cary, H. B. 1979. *Modern Welding Technology*. Prentice-Hall, Inc., Englewood Cliffs, N.J., pp.169–178.
13. Ando, K. 1967. Control method of automatic arc welding. *J. Japan Welding Society* 36(5): 78–88.
14. Ando, K., Nishiguchi, K., and Fukuda, K. 1967. Temperature characteristics of the droplet detaching from the wire tip in MIG welding — effect of Joule's heating. *J. Japan Welding Society* 36(10): 59–66.
15. Tsai, M. C., and Kou, S. 1990. Electro-

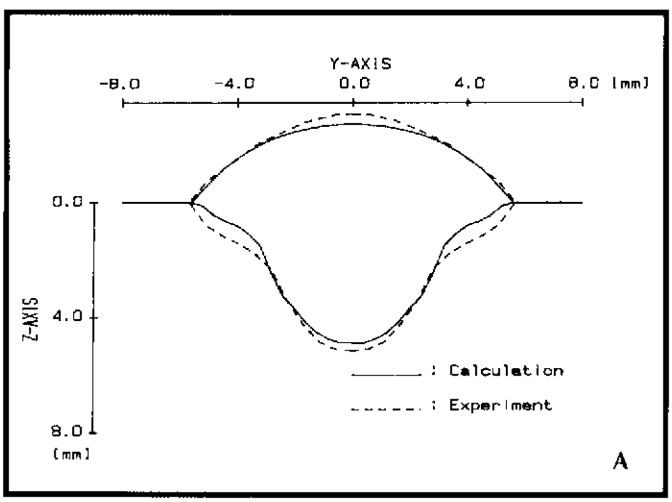

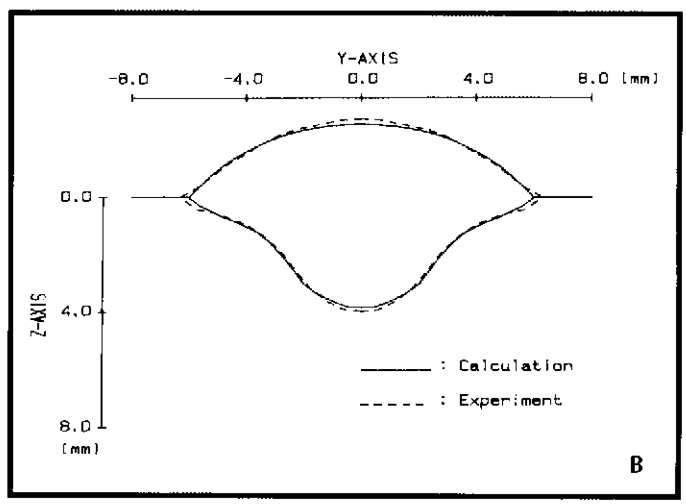

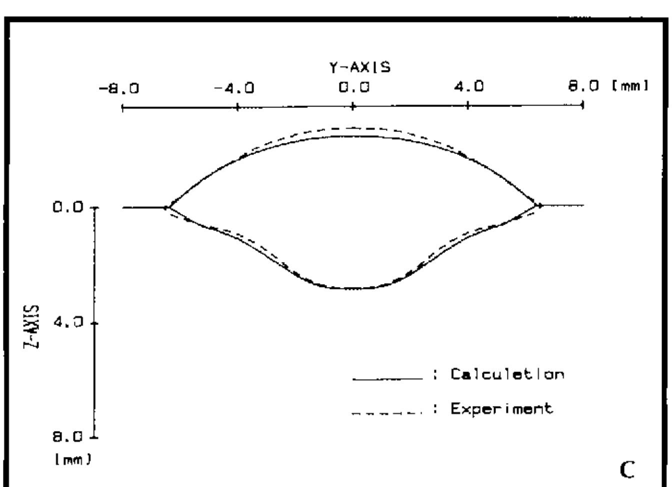

Fig. 16 — Comparisons of calculated weld shapes with experimental ones. A — L = 15 mm; B — L = 20 mm; C — L = 25mm.

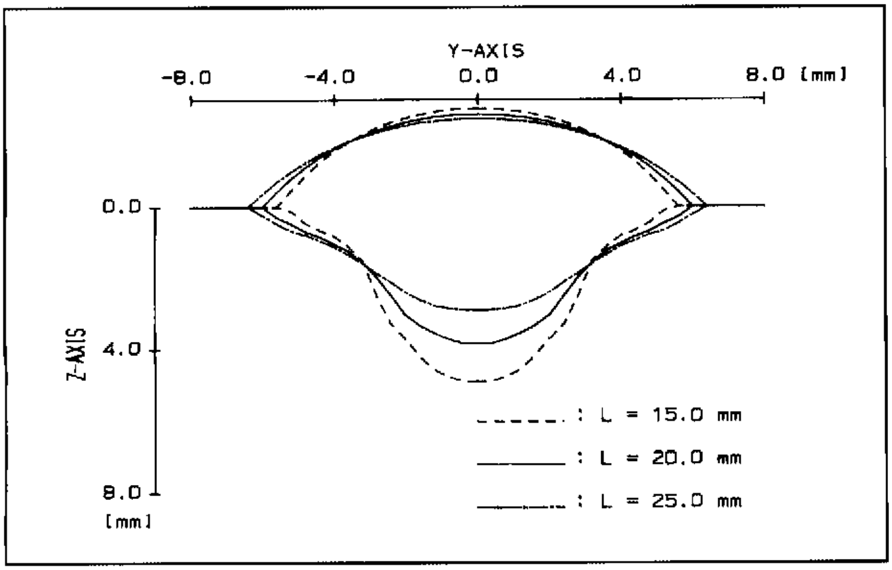

Fig. 17 – Effect of contact tube-to-workpiece distance on calculated weld shape.

magnetic force induced convection in weld pools with a free surface. *Welding Journal* 69(6): 241-s to 246-s.

16. Touloukian, Y. S. 1967. *Thermophysical Properties of High Temperature Solid Materials*. Vol. 3. The Macmillan Co., New York, N.Y.

17. Na, S. J., and Lee, S. Y. 1987. A study on the three-dimensional analysis of the transient temperature distribution in gas tungsten arc welding. *Proc. Inst. Mech. Engrs. Part B — J. Engineering Manufacture* 201:149–156.

18. Landau, L. D., and Lifshitz, E. M. 1959. *Fluid Mechanics*. Pergamon Press, Oxford, U.K.

19. Lin, M. L., and Eagar, T. W. 1985. Influence of arc pressure on weld pool geometry. *Welding Journal* 64(6): 163-s to 169-s.

20. Lin, M. L., and Eagar, T. W. 1986. Pressures produced by gas tungsten arcs. *Metal. Trans.* 17B(9): 601–607.

21. Haug, E. J. and Arora, J. S. 1979. *Applied Optimal Design*. John Wiley & Sons, New York, N.Y.

22. Vanka, S. P., Chen, B. C.-J., and Sha, W. T. 1980. A semi-implicit calculation procedure for flows described in boundary fitted coordinate systems. *Numerical Heat Transfer* 3: 1–19.

23. Patankar, S. V. 1980. *Numerical Heat Transfer and Fluid Flow*. McGraw-Hill, New York, N.Y.

24. Jang, D. S., Jetli, R., and Acharya, S. 1986. Comparison of the PISO, SIMPLER, and SIMPLEC algorithms for the treatment of the pressure-velocity coupling steady flow problems. *Numerical Heat Transfer* 10: 209–228.

25. Kim, J. W., and Na, S. J. 1991. A study on the three-dimensional analysis of heat and fluid flow in gas metal arc welding using boundary-fitted coordinates. *Proc. of ASME Symposium on Welding and Joining Processes*, 1991 ASME Winter Annual Meeting, PED-Vol. 51, Atlanta, Georgia, pp. 159–173.

26. Tsai, N. S., and Eagar, T. W. 1985. Distribution of the heat and current fluxes in gas tungsten arcs. *Metall. Trans.* 16B(12): 841–846.

Appendix

Nomenclature

a	effective radius of heat density distribution of arc
b	effective radius of current density distribution of arc
B	magnetic flux vector
c	effective radius of pressure distribution of arc
c	*specific heat*
e	*effective radius of velocity distribu tion of molten electrode*
f	*body force vector*
g	*gravitational acceleration*
H	*depth of solution domain*
I	*welding current*
J	*current density vector*
k	*thermal conductivity*
L	*tube-to-workpiece distance*
n	*normal unit vector of weld pool surface*
P_{max}	*maximum value of arc pressure distribution*
Q	*effective heat input*
q_a	*heat density distribution of arc* $=3Q/\pi a^2 \exp\{-3(r/a)^2\}$
r,z,θ	*coordinate system of moving heat source*
t_1	*tangential unit vector parallel to x-z plane*
t_2	*tangential unit vector parallel to y-z plane*
T_ℓ	*liquidus temperature of weld metal*
T_υ	*maximum temperature of weld pool surface*
T_∞	*ambient temperature*
U	welding speed
V	velocity vector
u,υ,w	x-, y-, z-component of velocity vector V
v_d	molten electrode droplet velocity at the weld pool surface
x,y,z	coordinate system of moving heat source

Greek Symbols

β	thermal expansion coefficient
Γ	diffusion coefficient
μ	viscosity
μ_m	magnetic permeability
ξ,η,ζ	transformed coordinates
ρ	density
dσ/dT	temperature gradient surface tension
∇	gradient operator

Superscripts

r,z,θ	r-, z-, θ–component of dependent vectors
x,y,z	x-, y-, z-component of dependent vectors

Subscripts

x,y,z	partial derivative with respect to x, y, z
ξ,η,ζ	partial derivative with respect to ξ, η, ζ